



HAL
open science

Backside Absorbing Layer Microscopy: Monolayer Counting in 2D Crystal Flakes

Dominique Ausserré, Refahi Abou Khachfe, Takashi Taniguchi, Kenji Watanabe, Fabien Vialla

► **To cite this version:**

Dominique Ausserré, Refahi Abou Khachfe, Takashi Taniguchi, Kenji Watanabe, Fabien Vialla. Backside Absorbing Layer Microscopy: Monolayer Counting in 2D Crystal Flakes. *physica status solidi (b)*, 2023, 10.1002/pssb.202300068 . hal-03858429v1

HAL Id: hal-03858429

<https://univ-lyon1.hal.science/hal-03858429v1>

Submitted on 17 Nov 2022 (v1), last revised 26 Jan 2024 (v2)

HAL is a multi-disciplinary open access archive for the deposit and dissemination of scientific research documents, whether they are published or not. The documents may come from teaching and research institutions in France or abroad, or from public or private research centers.

L'archive ouverte pluridisciplinaire **HAL**, est destinée au dépôt et à la diffusion de documents scientifiques de niveau recherche, publiés ou non, émanant des établissements d'enseignement et de recherche français ou étrangers, des laboratoires publics ou privés.

BALM : Monolayer counting in 2D crystal flakes.

Dominique Ausserré^{1,*}, Refahi Abou Khachfe², Takashi Taniguchi³, Kenji Watanabe³, Fabien Vialla^{4,*}

¹ Institut des Matériaux et Molécules du Mans UMR 6283, Le Mans Université, 72085 Le Mans, France

² Lebanese university, Faculty of technology, Hisbe Street, Saida, Lebanon

³ National Institute for Materials Science, 1-1 Namiki, Tsukuba 305-0044, Japan

⁴ Institut Lumière Matière UMR 5306, Université Claude Bernard Lyon 1, CNRS, Université de Lyon, 69622 Villeurbanne, France

*corresponding authors:

Dominique Ausserré *dominique.ausserre@univ-lemans.fr*

Fabien Vialla *fabien.vialla@univ-lyon1.fr*

Abstract

The properties of two-dimensional (2D) material stacks critically depend on the number of monolayers (m) in the stack. It is therefore important to quantify this number, which is a local quantity since 2D stacks are essentially heterogeneous. Optical interferential techniques based on contrast enhancing surfaces may be sensitive enough to visualize m variations but experimental determination of m requires heavy and unstable comparisons with multiparameter numerical models. Focusing on the recent Backside Absorbing Layer Microscopy, the most sensitive to date among interferential techniques, we demonstrate a self-calibrating method allowing instantaneous monolayer counting all over the sample surface which does not require the knowledge of the instrumental parameters, the sample or ambient refractive indices or the detailed structure of the contrast enhancing layer. The method is introduced step by step using examples of hexagonal Boron Nitride (hBN) stacks with increasing complexity. Exact monolayer counting up to 36 hBN monolayers is obtained using basic image analysis.

The properties of 2D crystals stacks are highly dependent of the number m of monolayers in the stack [MasBallestte2011, Xu2013]. Therefore, whether it is for the study or for the use of their properties, rapid counting of m is an important issue. The most popular and the simplest way to obtain few-layers stacks on an arbitrary support consists in repeated mechanical exfoliation of a bulk crystal followed by dry transfer to the substrate with the help of a tape or a polymer film [Novoselov2014]. It generally produces heterogeneous samples. Flakes a few tens of microns wide are obtained, with inside a number of atomically flat regions a few microns wide and limited by sharp steps. Similarly, growth techniques yield surfaces where terraces or puddles can locally modify the number of layers [Chen2015, Uchida2017]. The optical methods used for m counting are demanding since, in addition with a high sensitivity, they must have a good lateral resolution. This essentially implies optical microscopy [Dong2019]. The microscopy techniques used so far are mainly optical absorption in transmitted light [Frisenda2017], micro-Raman spectroscopy [Stenger2017, YouShinNo2017] or other spectroscopic and colorimetric imaging techniques [Dong2019, Hutzler2020] and optical interferential methods in reflected light [Novoselov2014]. Optical absorption is especially simple but it does not apply to non-absorbing materials such as Graphene Oxide (GO) or hexagonal Boron Nitride (hBN). Raman is the gold standard and provides information much beyond counting but it is limited to small m , the vibrational properties of the probed material must be previously known, the technique is slow because of the wavelength scanning and the measurement is strongly perturbed by the presence of other species. The same limitations apply to all other spectroscopic imaging methods. Interferential microscopy was applied to the characterization of graphene layers since the seminal paper by Novoselov and coworkers [Novoselov2014]. It is fast and simple and remains widely used. In order to reach monolayer sensitivity, Anti-Reflective (AR) surfaces are used as supporting plates. Most often, these are silicon surfaces covered with a silicon oxide layer. The Michelson contrast $C = (R_{stack} - R_{back}) / (R_{stack} + R_{back})$ of the stacks, is maximal whatever the intensity R_{stack} reflected by the stack when the background reflectivity R_{back} is minimal. This is obtained when the thickness of the AR layer is $e_{layer} = (1 + 2l)\lambda / 4n_{layer}$, with λ the wavelength of light, n_{layer} the layer refractive index and l an integer, which in practice is chosen to be either zero or one for graphene observation, leading to 100 and 300 nm thick silica layers. The technique can be further improved by optimizing the refractive index of the AR layer, according to the AR layer index rule $n_{layer} = \sqrt{n_{ambient}n_{solid}}$, with n_{solid} and $n_{ambient}$ the refractive index of the solid and the ambient medium. A number of authors reported improved interferential sensitivity by playing with the chemical nature of the layer material [Jung2007, Velicky2018]. Finally, neither the thickness nor the index condition can be satisfied for every wavelength so that spectral filtering is another important leverage [Golla2013]. In 2014, another family of AR layers was identified [Ausserré2014]. They are made of ultrathin layers of highly absorbing (most often conducting) materials, named ARA layers with the added A for "Absorbing". They must be used in reflected light on the back surface of a transparent window, that it is to say on an inverted microscope, otherwise they lose their AR properties. In these conditions, which characterize the so-called Backside Absorbing Layer Microscopy (BALM), they provide unparalleled sensitivity to minute material deposition. This was demonstrated in the context of 2D material studies [Campidelli2017, Jaouen2019], to explore electrochemical properties of nanoparticles [Lemineur2018, Lemineur2019, Lemineur2020] and to monitor the formation of biomembranes [Bompard2021]. When the 2D material under study is strongly absorbing, the sample itself can play the role of the ARA layer, so that a small number of layers appears with a high negative contrast on a transparent substrate in the said inverted geometry, as was demonstrated with graphene [WanLi2016].

When using interferential methods to count monolayers in a stack, the measured reflectivity is compared to a numerical model which is intended to reproduce it. However, this reflectivity is affected by a large number of parameters [Mondal2022] including the complex refractive index of the ARA layer

and of the sample, their dispersion, the ARA layer thickness, the spectrum of the source, the numerical aperture of the microscope, the spectral efficiency of the sensor, the presence of non-specular contributions (scattered light), the presence of parasitic contributions (added light) and the exact focus adjustment. It is also highly dependent of the optical constants of the probed material itself, which may fluctuate in a large extend from one sample to another [Kröner2020]. In addition, the optical characteristics of the contrast layer may not be exactly reproduced from one ARA surface to the other. Altogether, measuring or adjusting all the instrumental parameters to correctly mimic the experimental data obtained with a well-known sample is already a challenge in itself [Menon2019], so that counting m with this method in a new/unknown sample is practically impossible. A common method is then to calibrate the optical signal with a complementary method such as SEM, TEM or AFM [Jaouen2019, Schué2016, Kim2015] with the drawback of experimental heaviness. To resume, methods allowing rapid and friendly determination of m using interferential microcopy are still lacking. Here, focusing on the BALM technique, we describe a method allowing a model-free determination of m in stacks of a pure 2D material. The method only requires the presence of several stacks or steps in a stack, preferentially including a monolayer step, and a white light or at least a bicolor light source. It does not require the knowledge of any of the previously listed instrumental parameters, since they are replaced by three “consolidated”, or effective, parameters per color channel. One of them is measured directly. Another one is extracted from the comparison of two color channels in the images of the stacks, i-e from a relative measurement. The third one is obtained from the integer character of m , that is to say from thickness quantization. The three parameters are then sufficient to convert the measured reflectivity R of every color channel or any combination of them in a universal function $f(R)$ which is a linear (in the sense of affine) function of m . The method is introduced step by step through a progressive analysis of few-layers stacks, exfoliated using thin polydimethylsiloxane (PDMS) films, of hexagonal boron nitride (hBN), one of the most challenging materials in terms of sensitivity [Gorbachev2011] due to their one-atom thickness and high bandgap.

Our method is based on the AR property of the ARA (or near-ARA, [Campidelli2017]) sample supporting surface, according to the setup illustrated in Figure 1a. In practice, this surface has a weak yet non zero reflection. When a very thin layer is added, the reflectivity varies. This is why we can see it. This variation may be negative or positive. In the first situation, said of negative contrast, the reflectivity will reach a minimum R_{min} for some value e_{min} of the layer thickness e , and then increase. It was shown in reference [AbouKhachfe2019] that for small e (and e_{min}) this variation is parabolic. In the second case, said of positive contrast, the variation $R(e)$ is also parabolic but the minimum of the parabola is not covered by experimental data because it would correspond to a negative layer thickness. This minimum is virtual and $e_{min} < 0$ is an extrapolation length. For the parabola to be entirely defined, another information than the position of the minimum is needed. Ignoring the peculiar case $e_{min} = 0$, it is given by the value R_0 of the reflectivity obtained for a zero thickness of the added layer, that is to say the reflectivity of the bare support. It can be directly measured in a region which is free of stacks. The three parameters R_0, e_{min}, R_{min} define in a unique way the parabola which is supporting all the data points. From reference [AbouKhachfe2019], the relationship between thickness and reflectivity can be written as:

$$\frac{R-R_{min}}{R_0-R_{min}} = \left(\frac{e}{e_{min}} - 1 \right)^2 \quad (1)$$

A remarkable property of Equation (1) is that the left member is a relative quantity, with considerable advantages compared to absolute quantities. For instance, it is conserved in a linear transform $R \rightarrow R' = aR + b$ affecting as well R, R_0 and R_{min} . As a consequence, the validity of Equation (1) is not lost when adjusting the contrast (constant a) and brightness (constant b) of the reflected images, either

through the camera settings or in a post-treatment. Such a transformation would not be allowed when comparing the experimental data with a numerical model.

It is useful for many reasons to consider a function of R which is a linear function of e . Therefore we write :

$$\frac{e}{e_{min}} = 1 - f(R) \quad \text{when } e < e_{min}$$

$$\frac{e}{e_{min}} = 1 + f(R) \quad \text{when } e > e_{min}$$

, where we have set $f(R) \equiv \sqrt{\frac{R-R_{min}}{R_0-R_{min}}}$, $f(R)$ and the argument of the square root being always positive. The two cases resume in:

$$e/e_{min} = 1 + f(R) * \text{sgn}(e - e_{min}) \quad (2)$$

, with sgn the sign function. In the next section, we shall show how this equation can be used for monolayer counting in dry-transferred hBN flakes onto a gold near-ARA window.

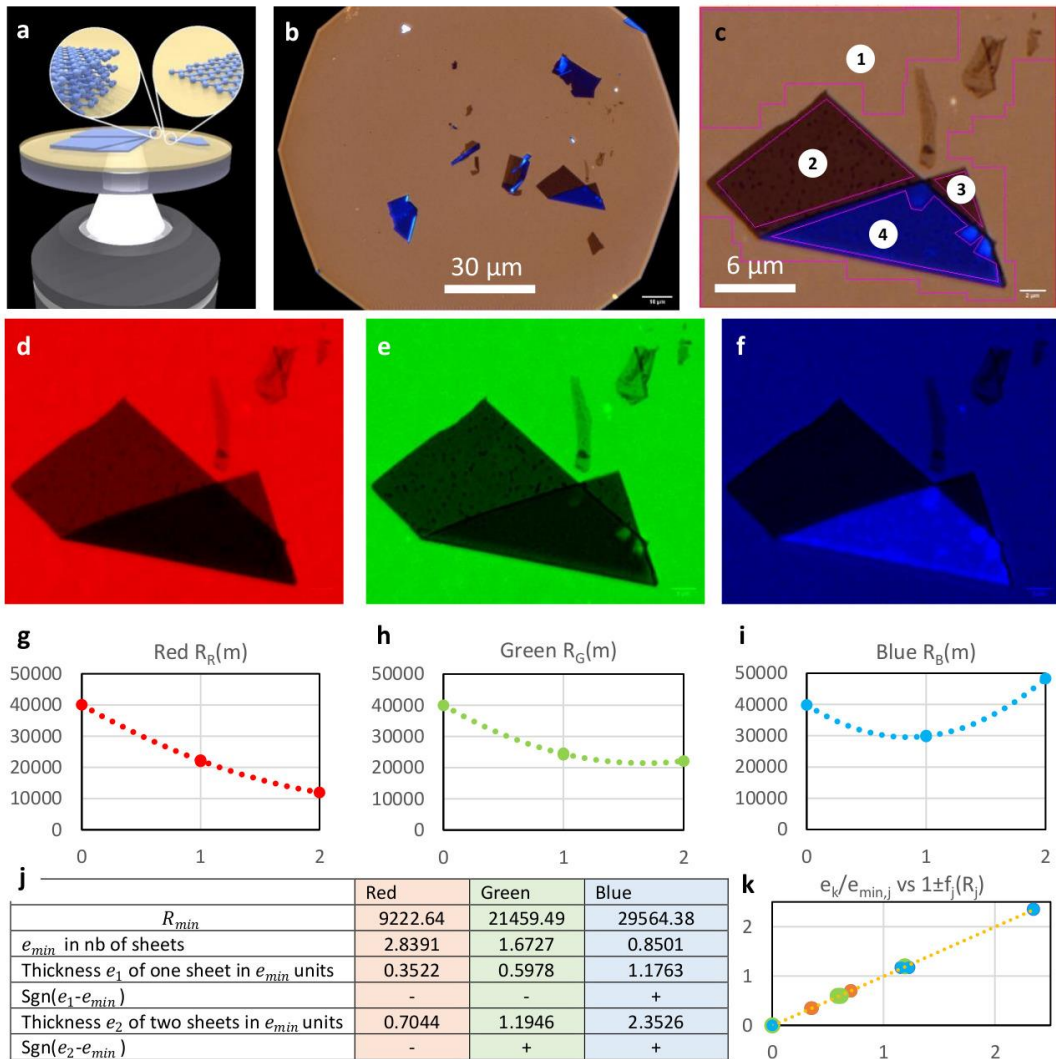


Figure 1. a : BALM experimental setup, where hBN flakes transferred on an gold ARA surface are monitored with white light from the backside of the window in an inverted optical microscope; b : Optical image of a given area on a sample with exfoliated hBN flakes; c : zoom on the studied folded sheet and numerical labelling of

regions; d-f : red, green and blue components of c, showing a contrast inversion in f; g-i : the three reflectivity levels as function of number of sheet (none, single and folded) and their fit with the best parabola; j : important numerical data, see text; k : the universal straight line e/e_{min} as a function of $1 + s(k) * f(R)$, see Eq. (3), with e_{min} , s , R and f different for each channel.

Figure 1b is a representative image of a first sample, with a few flakes dispersed on the gold surface. In such samples, we often find either folded or partially superimposing flakes, making possible to match m additions with intensity variations. Here we have a large regular folded sheet with a 10 μm typical size. This region is enlarged in Figure 1c. Since we use a color CCD camera, there are three independent images, shown in Figures 1d-f. We define four zones corresponding respectively to the bare substrate, the two parts of the single sheet and the folded sheet. The average intensity in each zone as a function of the number of sheets is plotted in Figures 1g-i, with the different curves corresponding to the Red, the Green and the Blue channels. Note that we ignore the number of monolayers in the sheet. Striking differences are observed, like a blue intensity larger with two sheets than with a single one, by contrast with the two other channels. With such a folding, the three measurements per color are sufficient to determine the three parabola, hence the three (different) $R_{min,j}$ values, with $j = R, G, B$ and the three $e_{min,j}$ values expressed in sheet units, or equivalently the thickness $e(k)$ of each zone ($k = 0,1,2$) expressed in $e_{min,j}$ units. The results are displayed in Figure 1j. From there, the sign of $[e(k) - e_{min,j}]$ is determined and we can use Equation (2) to plot $e(k)/e_{min,j}$ as a function of the transformed reflectivity $f_j[R_j(k)] = \sqrt{\frac{R_j(k) - R_{min,j}}{R_{0,j} - R_{min,j}}}$, as shown in Figure 1k. The data from the three channels perfectly align on a single straight line. The function f_j is different for each channel and parametrized by the values of $R_{min,j}$ and $R_{0,j}$. Figure 1k is a perfect illustration of Equation (2), that we rewrite with the color index j and the rank k of a zone made explicit :

$$e(k)/e_{min,j} = 1 + s_j(k) * f_j[R_j(k)] \quad (3)$$

, where $s_j(k) \equiv \text{sgn}[e(k) - e_{min,j}]$. We note $g_j(k)$ the right member of Eq. (3). When the latter holds, the ratio $g_{j1}(k)/g_{j2}(k)$ is constant ($= e_{min,j2}/e_{min,j1}$) for all k 's, $j1$ and $j2$ referring to two different color channels. This proportionality is achieved when and only when the values of $R_{min,j1}$ and $R_{min,j2}$ are correct. As a consequence, $R_{min,j1}$ and $R_{min,j2}$ may be found by fitting the constant ratio of the two quantities. Figures 2a-c show the best linear fits simultaneously obtained with every pair among the $g_R(k)$, $g_G(k)$ and $g_B(k)$ functions. The $R_{min,j}$ values found with this method are 9222, 21459 and 29564, slightly different from the previous ones issued from the parabolic fit, which were 9223, 21510 and 29485. The largest correction, on the blue channel, is about 0.3 %. This linear determination has many assets compared to the parabolic one: i) it does not require the knowledge of any relationship between the $e(k)$ values as the one provided by the folding between $e(k_1)$ or $e(k_3)$ and $e(k_2)$, nor any knowledge about these values; ii) it is more precise because the number of adjustable parameters is lower with a linear fit than parabolic; iii) it can be achieved by the eye, which is a fast and effective instrument to recognize straight lines. Note however that it yields only the $R_{min,j}$ quantities and not the $e_{min,j}$. When something is known about the $e(k)$ values as for the example in Figure 1 with the folded nature of the sheet, a parabolic fit with fixed $R_{min,j}$ may be achieved in a second step, yielding precisely the $e_{min,j}$, then the $s_j(k)$ values. The knowledge of $s_j(k)$ finally allows to plot the universal function $g_j(k)$ as in Figure 1g. When nothing is known about the $e(k)$ values, $s_j(k)$ must be chosen in each measured zone such that $g_j(k)$ is a single straight line for any given color index j . This difficulty is also present whenever we add a new measured zone, as discussed in the following.

In Figure 2, we extend the measurements to the stacks that were previously neglected in the zoom image. They make zones 5 to 9 in Figure 2d. They are small and weakly contrasted.

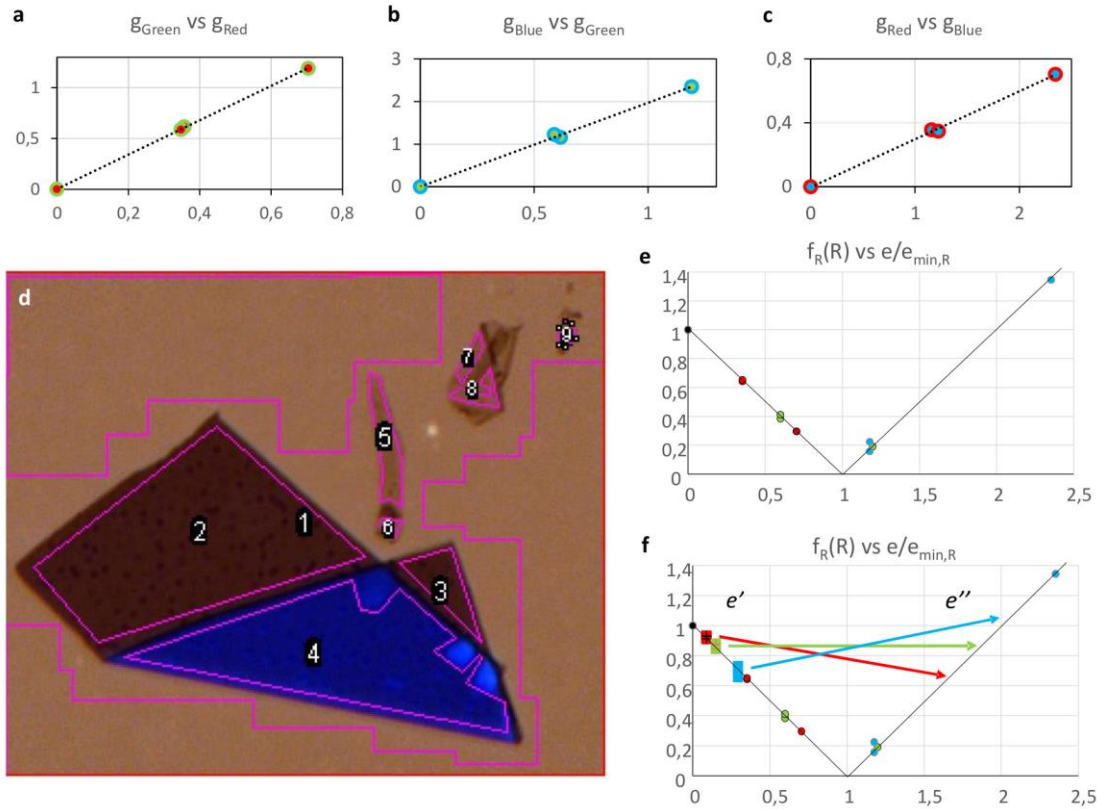


Figure 2. a-c : the best linear fits obtained after $(R_{min,j1}, R_{min,j2})$ adjustment by pairs, with $(j1, j2) \in \{R, G, B\}^2$; d : Same stack as in Figure 1b with added measurement zones 5 to 9; e : Universal curve $f_j[R_j(k)]$ as a function of $e(k)/e_{min,j}$ before introduction of the new dots; f : same after introduction of the new dots. The arrows illustrate the inversion of the red, green and blue dots ordering when switching from one branch to the other. To a given value of the ordinate $f_{j1}[R_{j1}(k)]$ corresponds two possible values $e'(k)/e_{min,j1}$ and $e''(k)/e_{min,j1}$ of the abscissa. These values hold only for one color channel, the green one in the Figure.

Figures 2e and 2f display the universal curve $f_j[R_j(k)]$ as a function of $e(k)/e_{min,j}$ before and after introduction of the new dots. The added f_j values are very close to each other, making a single cluster per channel, and should correspond to the same number k_u . The width of this cluster is due to zone 9, which area is only $1 \mu\text{m}^2$, with important edge effects. We could have legitimately ignored it. By contrast with the graph of $g_j(k)$ shown in Figure 1f, the curve is not monotonic, the ignored sign $s_j(k)$ in $g_j(k)$ resulting in a degeneracy of $e(k)/e_{min,j}$, which means that to the added value $R_j(k_u)$ of the reflectivity, hence to the added ordinate $f_j[R_j(k_u)]$ on the universal curve, correspond two possible values $e'(k_u)/e_{min,j}$ and $e''(k_u)/e_{min,j}$ of the adimensional thickness, located on each side of the minimum $[1,0]$. To decide which is the good one, we recall the order relationship $e_{min,R} > e_{min,G} > e_{min,B}$, see Figure 1h-i. It follows that $e(k)/e_{min,R} < e(k)/e_{min,G} < e(k)/e_{min,B}$, meaning that the red, the green and the blue dots associated to a same zone k are always ordered from left to right on the universal curve. Due to the slope inversion at $e/e_{min} = 1$, the same dots are ordered from top to bottom on the left branch $e/e_{min} < 1$ and from bottom to top on the right branch $e/e_{min} > 1$. This ordering inversion is materialized by the colored arrows in Figure 2f. It is worth highlighting that if a given value of R_{j1} on one channel (R_G in the figure) has two arguments e' and e'' , these two solutions

will not generate the same R_{j2} for $j2 \neq j1$ (R_R or R_B in the figure). In other words, the degeneracy holds only for one channel. Thus it is lifted by comparing the values of $f_j[R_j(k_u)]$ for $j1$ and $j2$. We take $j2 = Red$ for instance. The added dots correspond to $f_R[R_R(k_u)] > f_G[R_G(k_u)]$. Therefore, they must be placed on the left branch. We finally get $k_u = 0,25$. Since k_u is an integer, its minimum possible value is 1. With $k_u = 1$, the reference brown sheet should be made of at least 4 monolayers. We could have as well $k_u = 2$ or $k_u = 3$ or any integer and the brown sheet made of 8, 16 or more monolayers, respectively. Extending the investigated number of flakes, as presented in Supplementary S1 by using systematically the method previously described, shows that the zones identified here as monolayers actually correspond to bilayers, i.e. $k_u = 2$. The unbiased mapping of the effective thickness $e(k)$ to an actual number of layer $m(k)$ is discussed and generalized in the following in a case without a folded sheet to anchor the process.

A new hBN sample made with similar mechanical exfoliation technique on top of a different ARA substrate is presented in Figure 3a. We combine several flakes extracted from several images taken with identical microscope settings into a single one to get a sufficient number of samples, which was allowed by the excellent homogeneity of our surface. Here we have no folding on which to anchor the m distribution. We proceed as before, i.e. dots ordering which fixes the sign $s_j(k)$, and then $R_{min,j}$ adjustment from color pair comparison of the $g_j(k)$. The approach to render the dots ordering automatic, including detection of repeated levels, is exposed in Supplementary Information S2. Our method presents similarities with the clustering algorithms used with the same purpose in artificial intelligence approaches [Yuhaoli2019, Sterbentz2021]. The remaining difficulty is to find the $m(k)$ values. For this purpose, we postulate a value m_p for an arbitrary chosen zone p . From equation (3), we get :

$$\frac{m(k)}{m_p} = \frac{g_j(k)}{g_j(p)} \quad (4)$$

The number of layers being quantized, $m(k)$ is ideally an integer number. This is strictly true if :

$$m(k) - INT\{m(k) + 0,5\} = 0$$

, with INT the integer function. Considering measurement uncertainty, our reasonable expectation is that the absolute value of the left member is much smaller than 1 for a majority of k values, from 1 to k_{Max} . Therefore, a good value of m_p will minimize the averaged squared distance of the $\{m(k)\}$ set from integer numbers :

$$\chi^2 \equiv (1/k_{Max}) \sum_{k=1}^{k_{Max}} \{m(k) - INT\{m(k) + 0,5\}\}^2 \quad (5)$$

Note that the effect of changing m_p for lm_p , with $l > 1$ an arbitrary integer, will change $m(k)$ for $lm(k)$ in the second member of Equation (5) and therefore multiply by l^2 the squared distance to the closest integer whenever this distance was already small ($\ll 0.5$). As a consequence, this expression will unfavor unnecessary high as well as too low m_p values.

With the new sample shown in Figure 3a, we were able to determine the exact number m of monolayers in the flakes, i.e. with a zero uncertainty, up to $m = 36$, a half-monolayer uncertainty appearing as a mismatch between the green channel and the two others with the 40th layer, which rank could also be 39 but not 41. The same procedure was also applied to another sample with results reported in Supplementary S3. They are comparable. However, the determination of the exact number of monolayers was limited to 10 layers due to higher pollution of the sample. Here the results are presented in Figure 3b where we have plotted $s_j(k) * \sqrt{R_j(k) - R_{min,j}}$ as a (non-universal) function of $m(k)$ (instead of $g_j(k)$) as a function of $m(k)/m_{min,j}$, after $R_{min,j}$ optimization. This is the simplest

function that we can linearize channel by channel in order to determine the $R_{min,j}$. It is effective as well and saves the introduction of $\sqrt{R_0 - R_{min,j}}$ in the denominator of $g_j(k)$, the former being in the present case a very small quantity for the blue channel. On the red and green channels, every experimental dot touches the fitted line, showing that the amplitude of the uncertainty is close to the dot diameter. Any change on m significantly alters the visual impression as well as the fit quality. Note that the extrapolated $m_{min,j}$ values, namely 3 (blue), 53 (green) and 109 (red), are quite different from the previous configurations (see S1 and S3), mainly due to different characteristics of the gold layer, to a different nature of the light source, and to a different setting of the microscope aperture hole. This huge variation in the $R_{min,j}$ values highlights the difficulty that would be encountered to fit the absolute experimental reflectivity with a theoretical model [Mondal2022], and by comparison the power of our self-calibrating method.

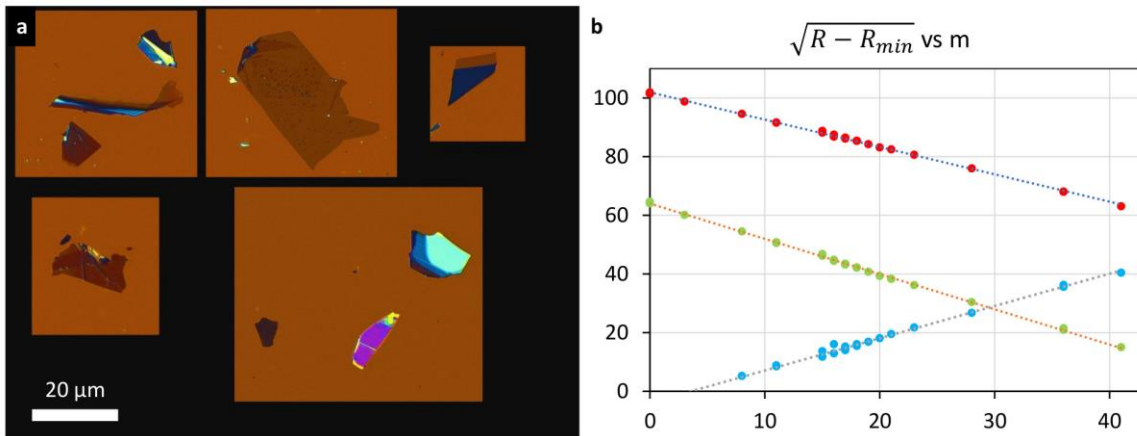


Figure 3 a: Patchwork of the exfoliated hBN stacks used in the measurements. The height of the full frame is 100 μm . The same scale applies to the different domains; b : the linear dependence of $s_j(k) * \sqrt{R_j(k) - R_{min,j}}$ as a function of m for the three channels after $R_{min,j}$ adjustment.

Once calibrated from the analysis of one image as explained in length in this work, the BALM technique allows instantaneous identification of m in any stack deposited on the same surface and observed using the same instrument with the same settings. Although not mandatory, a very favorable condition for a safe counting is the presence of at least one monolayer in the observed steps. In figure 3b, we have 6 such consecutive monolayer steps and also several 2 and 3 layers steps, making the counting very sound. It is worth emphasizing that quantization plays an essential role in the determination of m because it allows an ensemble adjustment. Would the local thickness not be quantized, we could not make the local thickness quantitative without the help of either a caliber or a cross-correlated AFM measurement. One could argue that a doubt may persist in the absence of such control about the correct identification of the monolayer, that it could be mixed with a bi- or tri-layer. However, extending the measurement to higher stacks provides us with another reference by taking us beyond the linear regime of the function f_j , or equivalently beyond the parabolic regime of R_j . When increasing the sample thickness m , R_j will exhibit an inflexion point, and then a maximum related to the optical wavelength according to thin film interferential behavior. This maximum can be used for an additional and independent optical calibration of the sample thickness as shown in Supplement S4. This maximum taken on the blue channel matches the expected number of layers estimated from the (still linear) red channel, confirming the correct identification of the unit monolayer. We underline that the effectiveness of this optical calibration is not affected by the characteristics of the contrast layer.

An important contribution to the uncertainty on m , evaluated in the present experiment from the mismatch between color channels (quantified in details in S3), is the presence of local dots decorating most of the flat zones. They can be identified as buried or adsorbed residues from the polymer used as exfoliation stamp or from atmospheric hydrocarbons [Schwartz2019, Gasparatti2020]. Their contribution to the average optical signal intensity of a zone is highly variable. It depends on m in this zone and most notably on the channel considered, as demonstrated in Supplement S5. We note that the limitation for the maximum unambiguous m -counting range is mainly due to the presence of these contaminants, even though in the present work, we tried to carefully exclude the remaining dots of adsorbed pollutants from the measurement zones. On the other side, the strong contrast yielded by our microscopy technique can be of high interest for the fast and easy observation of such contaminants in hBN stacks, which is crucial when building heterostructures [Gasparatti2020].

An interesting prospective possibility is a combination of our approach and of a model based analysis. Instead of predicting the absolute reflectivity, the numerical model would be used to generate the three consolidated parameters (per channel) which are effective in the analysis, the latter forming an intermediate stage between the plethora of hardly controlled experimental parameters and the measured quantities. Then their dependence with a chosen physical parameter could be evaluated from the numerical model. The first additional information expected along this route would be the measurement of the sample refractive index (see S4 as an example), whose knowledge is of high importance for modeling the optical and electronic properties of 2D material nanostructures [Raja2017, Laturia2018].

Last but not least, all the operations described in our treatment can be implemented as real time image processing tools, allowing the live counting of monolayers in 2D material stacks.

Acknowledgments

This work was partially supported by ANR through project SoftNanoflu (ANR-20-CE09-0025)

Conflict of Interest

The authors have no conflicts to disclose.

References

Mas-Balleste 2011

Ruben Mas-Balleste, Cristina Gomez-Navarro, Julio Gomez-Herrero and Felix Zamora, 2D materials: to graphene and beyond, *Nanoscale*, 2011, **3**, 20-30

Xu 2013

Mingsheng Xu, Tao Liang, Minmin Shi, and Hongzheng Chen, Graphene-Like Two-Dimensional Materials, *Chem. Rev.* 2013, **113**, 3766–3798

Novoselov 2004

K. S. Novoselov, A. K. Geim, S. V. Morozov, D. Jiang, Y. Zhang, S. V. Dubonos, I. V. Grigorieva, A. A. Firsov, Electric Field Effect in Atomically Thin Carbon Films, *Science* 2004, **306**, 666-669

Chen 2015

Xiangping Chen, Lili Zhang, Shanshan Chen, Large area CVD growth of graphene *Synthetic Metals Part A* 2015, **210**, 95-108

Uchida 2017

Yuki Uchida, Tasuku Iwaizako, Seigi Mizuno, Masaharu Tsuji and Hiroki Ago, Epitaxial chemical vapour deposition growth of monolayer hexagonal boron nitride on Cu(111)/sapphire substrate, *Phys. Chem. Chem. Phys.* 2017, **19**, 8230-8235

Dong 2019

Xingchen Dong, Ali K. Yetisen, Michael H. Köhler, Jie Dong, Shengjia Wang, Martin Jakobi, Xiaoxing Zhang, and Alexander W. Koch, Microscale Spectroscopic Mapping of 2D Optical Materials, *Adv. Optical Mater.* 2019, 1900324 (20pp)

Frisenda 2017

Riccardo Frisenda, Yue Niu, Patricia Gant, Aday J Molina-Mendoza, Robert Schmidt, Rudolf Bratschitsch, Jinxin Liu, Lei Fu, Dumitru Dumcenco, Andras Kis, David Perez De Lara and Andres Castellanos-Gomez, Micro-reflectance and transmittance spectroscopy: a versatile and powerful tool to characterize 2D materials *J. Phys. D: Appl. Phys.* 2017, **50**, 074002 (8pp)

Stenger 2017

I. Stenger, L. Schué, M. Boukhicha, B. Bérini, B. Plaçais, A. Loiseau and J. Barjon. Low frequency Raman spectroscopy of few-atomic-layer thick hBN crystals. *2D Materials*, IOP Publishing, 2017, **4** (3), pp.031003.

You-Shin No 2017

You-Shin No, Hong Kyw Choi, Jin-Soo Kim, Hakseong Kim, Young-Jun Yu, Choon-Gi Choi and Jin Sik Choi, Layer number identification of CVD-grown multilayer graphene using Si peak analysis, *Scientific Reports* 2018, **8** : 571 pp 1-9
DOI:10.1038/s41598-017-19084-1

Hutzler 2020

Andreas Hutzler, Birk Fritsch, Christian D. Matthus, Michael P. M. Jank and Mathias Romme, Highly accurate determination of heterogeneously stacked Van-der-Waals materials by optical microspectroscopy. *Scientific Reports* 2020, **10**:13676 | <https://doi.org/10.1038/s41598-020-70580-3>

Jung 2007

Inhwa Jung, Matthew Pelton, Richard Piner, Dimitiy A. Dikin, Sasha Stankovich, Supinda Watcharotone, Martina Hausner, and Rodney S. Ruoff, Simple Approach for High-Contrast Optical Imaging and Characterization of Graphene-Based Sheets. *Nanoletters* 2007, **7** (12) pp 3569-3575

Velicky 2018

Matěj Velický, William R Hendren, Gavin E Donnelly, Joel M Katzen, Robert M Bowman and Fumin Huang, Optimising the visibility of graphene and graphene oxide on gold with multilayer heterostructures. *Nanotechnology* 2018, **29** (27), 275205 and Corrigendum, *Nanotechnology* 2019, **30** 439501

Golla 2013

Dheeraj Golla, Kanokporn Chattrakun, Kenji Watanabe, Takashi Taniguchi, Brian J. LeRoy, and Arvinder Sandhu, Optical thickness determination of hexagonal boron nitride flakes. *Appl. Phys. Lett.* 2013, **102**, 161906 (3 pages)

Ausserré 2014

D. Ausserré, R. Abou Khachfe, L. Roussille, G. Brotons, L. Vonna, F. Lemarchand, M. Zerrad, and C. Amra, Anti-Reflecting Absorbing Layers for Electrochemical and Biophotonic Applications *J Nanomed Nanotechnol* 2014, **5** (4);

Campidelli 2017

S. Campidelli, R. Abou Khachfe, C. Amra, M. Zerrad, R. Cornut, V. Derycke, D. Ausserré, Backside Absorbing Layer Microscopy: Watching Graphene Chemistry *Science Advances* 2017, **3** (5), e1601724

Jaouen 2019

K. Jaouen, R. Cornut, D. Ausserre, S. Campidelli, V. Derycke
Ideal optical contrast for 2D materials observation using bi-layer antireflection absorbing substrates
Nanoscale 2019, **13**, pp 1-3 | 1 <https://doi.org/10.1039/C8NR09983A>

Lemineur 2018

J.-F. Lemineur, J. -M. Noël, D. Ausserré, C. Combellas, F. Kanoufi, Combining electrodeposition and optical microscopy for probing size-dependent single nanoparticle electrochemistry.
Angewandte Chemie, Communication 2018
<https://doi.org/10.1002/anie.201807003>

Lemineur 2019

J.-F. Lemineur, J. -M. Noël, C. Combellas, D. Ausserré, and F. Kanoufi, The promise of antireflective gold electrodes for optically monitoring the electro-deposition of single silver nanoparticles
Faraday Discuss., 2018,210, 381-395
<https://doi.org/10.1039/C8FD00037A>

Lemineur 2020

J.-F. Lemineur, J. -M. Noël, A. Courty, D. Ausserre, C. Combellas, F. Kanoufi, In Situ Optical Monitoring of the Electrochemical Conversion of Dielectric Nanoparticles: From Multistep Charge Injection to Nanoparticle Motion. *J. Am. Chem. Soc.* 2020, **142** (17), pp 7937–7946

Bompard 2021

J. Bompard, O. Maniti, R. Abou Khachfe, D. Ausserré, A. Girard-Egrot, BALM: Watching the Formation of Tethered Bilayer Lipid Membranes with submicron lateral resolution,
Langmuir 2021, **37** (31), 9457–9471
<https://doi.org/10.1021/acs.langmuir.1c01184>

Wan Li 2016

Wan Li, Seonah Moon, Michal Wojcik, and Ke Xu, Direct Optical Visualization of Graphene and Its Nanoscale Defects on Transparent Substrates,
Nano Lett. 2016, **16**, pp 5027–5031
DOI: [10.1021/acs.nanolett.6b01804](https://doi.org/10.1021/acs.nanolett.6b01804)

Mondal 2022

Mainak Mondal, Ajit K. Dash and Akshay Singh, Optical Microscope Based Universal Parameter for Identifying Layer Number in Two-Dimensional Materials,
ACS Nano 2022, **16** (9), 14456–14462

Kröner 2020

Anton Kröner and Thomas Hirsch, Current Trends in the Optical Characterization of Two-Dimensional Carbon Nanomaterials,
Frontiers in Chemistry 2020, **7**, pp 1-14 | Article 927

Menon 2020

Thanmay S Menon, Simli Mishra, Vidhu Catherine Antony, Kiranmayi Dixit, Saloni Kakkar, Tanweer Ahmed , Saurav Islam, Aditya Jayaraman, Kimberly Hsieh, Paritosh Karnatak and Arindam Ghosh, Optimising graphene visibility in van der Waals heterostructures.
Nanotechnology 2019, **30**, 395704 (7pp)

Schué 2016

L. Schué, B. Berini, A.,C. Betz, B. Plaçais, F. Ducastelle, J. Barjon and A. Loiseau, Dimensionality effects on the luminescence properties of hBN.
Nanoscale 2016, **8**, 6986

Kim 2015

Dong Hyun Kim, Sung-Jo Kim, Jeong-Seon Yu, and Jong-Hyun Kim, Measuring the Thickness of Flakes of Hexagonal Boron Nitride Using the Change in Zero-Contrast wavelength of Optical Contrast.

Journal of the Optical Society of Korea 2015, **19** (5) pp. 503-507

Gorbachev 2011

R. V. Gorbachev, I. Riaz, R. R. Nair, R. Jalil, L. Britnell, B. D. Belle, E. W. Hill, K. S. Novoselov, K. Watanabe, T. Taniguchi, A. K. Geim, P. Blake, Hunting for Monolayer Boron Nitride: Optical and Raman Signatures, *Small* 2011, **7** (4), pp 465-468

Abou Khachfe 2020

R. Abou Khachfe and D. Ausserre, Backside Absorbing Layer Microscopy: A universal relationship between physical thickness and reflectivity, *Optics Express* 2020, **28** (4) / 17 pp 4836-4844

Yuhao Li 2019

Yuhao Li, Yangyang Kong, Jinlin Peng, Chuanbin Yu, Zhi Li, Penghui Li, Yunya Liu, Cun-Fa Gao, Rong Wu. Rapid identification of two-dimensional materials via machine learning assisted optic microscopy, *Journal of Materiomics* 2019, **5**, pp 413-421

Sterbentz 2021

Randy M. Sterbentz, Kristine L. Haley and Joshua O. Island, Universal image segmentation for optical identification of 2D materials *Scientific Reports* 2021, **11**:5808 (8 pages)

Schwartz 2019

Jeffrey J. Schwartz, Hsun-Jen Chuang, Matthew R. Rosenberger, Saujan V. Sivaram, Kathleen M. McCreary, Berend T. Jonker, and Andrea Centrone, Chemical Identification of Interlayer Contaminants within van der Waals Heterostructures, *ACS Appl. Mater. Interfaces* 2019, **11**, pp 25578–25585

Gasparutti 2020

Isabella Gasparutti, Seung Hyun Song, Michael Neumann, Xu Wei, Kenji Watanabe, Takashi Taniguchi, and Young Hee Lee, How Clean Is Clean? Recipes for van der Waals Heterostructure *Cleanliness Assessment*, *ACS Appl. Mater. Interfaces* 2020, **12**, 7701–7709

Raja 2017

Archana Raja, Andrey Chaves, Jaeun Yu, Ghidewon Arefe, Heather M. Hill, Albert F. Rigosi, Timothy C. Berkelbach, Philipp Nagler, Christian Schüller, Tobias Korn, Colin Nuckolls, James Hone, Louis E. Brus, Tony F. Heinz, David R. Reichman and Alexey Chernikov, Coulomb engineering of the bandgap and excitons in two-dimensional materials, *NATURE COMMUNICATIONS* | **8**:15251 | DOI: 10.1038/ncomms15251

Laturia 2018

Akash Laturia, Maarten L. Van de Put and William G. Vandenberghe, Dielectric properties of hexagonal boron nitride and transition metal dichalcogenides: from monolayer to bulk. *npj 2D Materials and Applications* (2018) **2**:6 ; doi:10.1038/s41699-018-0050-x

Supplementary S1

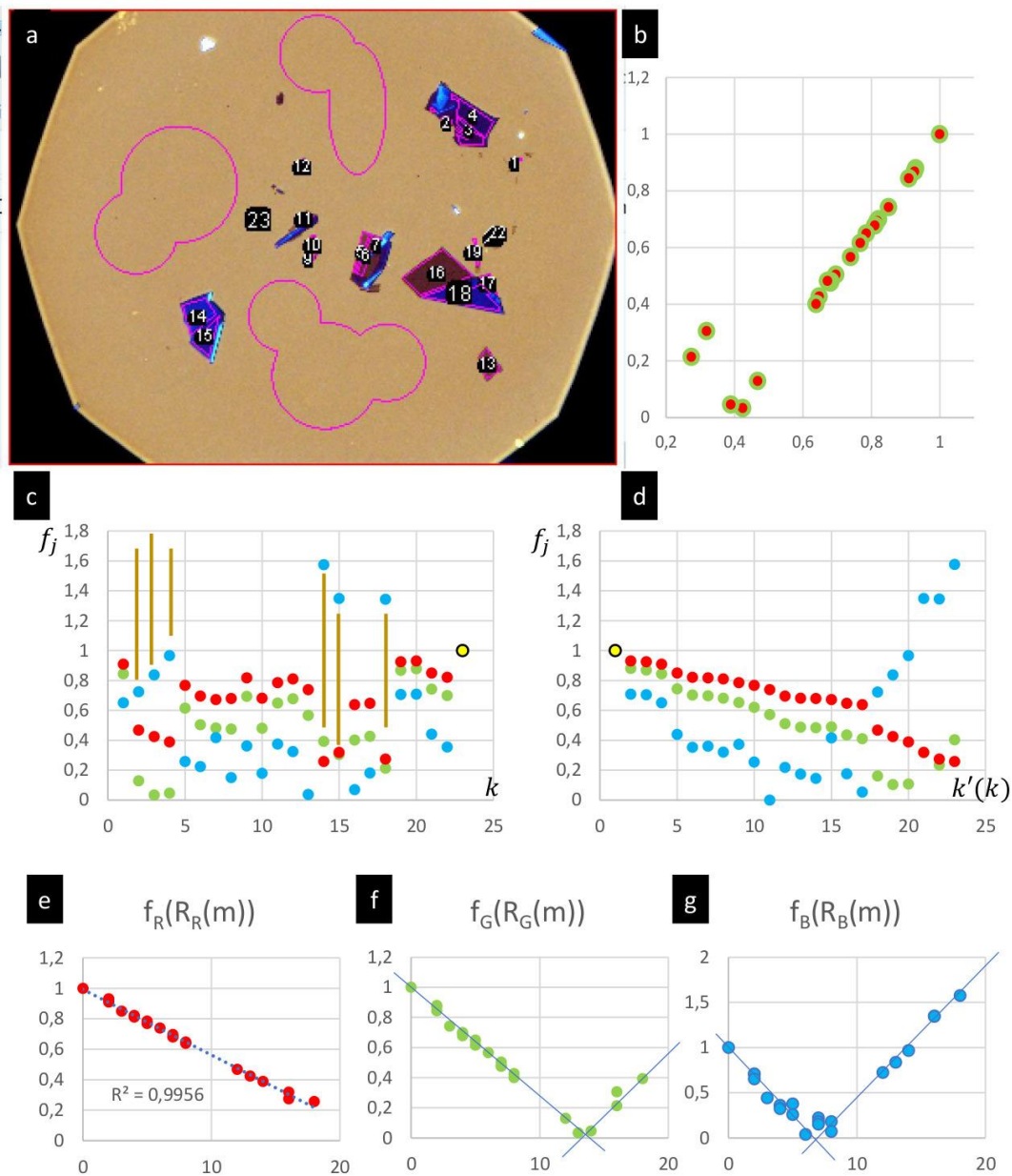


Figure S1 a : The 23 measurement zones in the entire 100 μm high image; b : plot of $f_G(R_G)$ versus $f_R(R_R)$ after adjustment of $R_{min,G}$ and $R_{min,R}$ in order to maximize the range of proportionality between the two signals; c : Plot of $f_j(R_j)$ as a function of k for $j = R, G, B$. Dots with Inverted R,G,B ordering are highlighted by orange vertical lines; d : Plot of $f_j(R_j)$ as a function of $k'(k)$ dictated by the decrease of the red signal; e : f-h : Plots of the three $f_j(R_j)$ as a function of m .

In Figure S1, we extend the measurements related to Figure 1 & 2 in main text to all the stacks or internal levels visible in the entire image, and sufficiently regular. New zones are shown in Figure S1a. To illustrate that our method applies for any image settings, we changed the dynamical range of each channel, i.e. the brightness and contrast levels, with respect to the previous images in main text. The previously determined values of R_{min} are no more valid. Figure S1a shows the measurement zones, labelled by k . The labels of the previously measured zones are respectively 23 for the bare gold

(yielding R_0 value), 19 and 20 for the presumed single monolayer, 16 and 17 for the reference single sheet, and 18 for the folded sheet. The first step is to determine the new values of the $R_{min,j}$. They are adjusted by optimizing by-piece the linearity of the pair-relationships between the three $f_j[R_j(k)]$. This method is effective when the number of zones is $\gg 5$, with two possible sign changes over the total range, hence the possible presence of 3 segments. Compared to $g_j(R_j)$, it does not involve any assumption on the sign $s_j(k)$. Figure S1b illustrates this step with the example of $f_G(R_G)$ vs $f_R(R_R)$ after adjustment of $R_{min,G}$ and $R_{min,R}$. Then the quantities $f_j(R_j)$ are determined. Compared to the R_j , the latter are just vertically rescaled data. Since f_j is a monotonic mapping, the f_j ordering vs k is the same as for R_j . This is not the case however for the ordering vs j . This why f_j is required in the following step. The result is shown for each zone and for the three channels in Figure S1c. The dots seem randomly distributed, but we recognize two ensembles. In the first one, with no mark, the f_j red-green-blue order corresponds to at least the red channel on the left branch. In the second one, marked by orange vertical lines, at least the blue dots are on the right branch. In the present case however, it is enough to re-order the results by decreasing values on the red channel because we have $e(k) < e_{min,R}$ for all k . This new order defines a mapping $k'(k)$ from 1 to 23. Figure 3d shows $f_j(R_j)$ as a function of k' . At this stage, we don't know how to convert k' into a thickness since we have no regular scale on the horizontal axis. The last step is to build it. For that, we define a second mapping $m[k'(k)]$ as the number of monolayers in zone k . We isolate the previously measured dots and set $m = 0, 1, 4, 8$ (respectively for the bare gold, presumed monolayer, single sheet and folded sheet) at the corresponding places on the horizontal axis. This defines as before one or two straight lines, depending on the channel. Then we adjust m for each zone such as the corresponding dot is located on the straight line. We find that a significant number of dots correspond to half-integer numbers, so we have to double all m values. The previous monolayer was therefore (at least) a bilayer and the single sheet was made of 8 layers. The results $f_j[R_j(m)]$ are shown for each channel in Figures 3e-g. The horizontal rescaling is now complete. The abscissa of each minimum can be expressed in terms of m . We have $m_{min,R} \cong 24$, $m_{min,G} \cong 14$ and $m_{min,B} \cong 7.5$ (being a virtual quantity, $m_{min,j}$ has not to be an integer number). By contrast with the $R_{min,j}$, the $m_{min,j}$ are independent of the brightness/contrast image settings. They provide solid landmarks when browsing a sample.

Supplementary S2

Here is introduced an alternative to the method used in Supplementary 1 in order to find the $R_{min,j}$ values, which is better suited for an automatic processing. It also includes thickness ordering of the data and detection of repeated levels.

$k = \{1, N_1\}$ is the rank of a measured zone. We know $R_{0,j}$ directly from the measurements but we cannot estimate $f_j[R_j(k)]$ as long as we ignore the $R_{min,j}$ values. Thus we set $\rho_{min,j} = \min_k[R_j(k)]$ and define $\varphi_j(k) = \sqrt{\frac{R_j(k) - \rho_{min,j}}{R_{0,j} - \rho_{min,j}}}$ as an approximation of f_j . Note that $\rho_{min,j} \geq R_{min,j}$ and that the minima of $R_j(k)$, $f_j(k)$ and $\varphi_j(k)$ are in correspondence, i.e. obtained for the same k .

We order the data according to decreasing $\varphi_R(k)$, or equivalently $R_R(k)$ values. This ordering defines a mapping $k'(k)$. In general, the variation of φ_G and φ_B with k' is not monotonic. To locate the different minima, we consider $\Delta\varphi_j(k') = \varphi_j(k' + 1) - \varphi_j(k')$, $\sigma_j(k') = \text{sgn}[\Delta\varphi_j(k')]$ and $\Sigma(k') = \sum_j \sigma_j(k')$. The possible values of Σ , depending on the position of the dots with respect to each minimum min_j , are summarized in table S1-1.

	<i>minB</i>		<i>minG</i>		<i>minR</i>	
σ_R	-1	-1	-1	-1	-1	-1
σ_G	-1	-1	+1	+1	-1	-1
σ_B	-1	+1	+1	+1	-1	-1
Σ	-3	-1	+1	+1	-3	-3

Table S1 Sign σ_j for the three channels in the four thickness zones delimited by the three reflectivity minima (one per channel). σ_R has a constant value due to Initial ordering according to R_R . Σ is the sum of the three signs.

The sign $\sigma_j(k')$ must reflect a significant change in $e(k')/e_{min,j}$. Indeed, when $e(k' + 1) = e(k')$, all the signs $\sigma_j(k')$ become random, governed by noise contributions. Repeated levels must be recognized and merged. For this purpose, we compare the cumulated squared variation $\Delta^2(k') = \sum_{j=R,G,B} \Delta\varphi_j^2(k')$ to an arbitrary threshold Δ_c^2 and we group all successive k' such as $\Delta^2(k') < \Delta_c^2$ while averaging their φ_j values. Δ_c^2 may be quite important, say for instance $6 * \Delta\varphi_R^2(k')$. Indeed, one term in $\Delta\varphi_j^2(k')$ may be weak because of a branch switching, but for the three terms in Δ^2 to be simultaneously weak, $e(k' + 1)$ and $e(k')$ must be identical. Once this process achieved, we are left with N different k' values instead of previously N_1 and we redistribute k' from 1 to N . Then we locate the measurements in the different branches with the help of a new mapping $k''(k')$ defined by $k'' = k' + N \left\lfloor \frac{\Sigma(k') + 3}{2} \right\rfloor$. Then $N < k'' < 2N$ corresponds to the dots located between *minB* and *minG* and $2N < k'' < 3N$ to the dots located between *minG* and *minR*. Only the dots in two extreme branches, below *minB* and above *minR*, remain mixed. They correspond to $k' < N$. We redistribute these values as follows : if $\varphi_R(k') < \varphi_G(k')$, then $k'' = k' + 3N$, otherwise $k'' = k'$. We end up with a total of four branches, all determined. Redistributing the k'' values used between 1 and N , we get the rank $k''(min_j)$ of each minimum, hence finally $s_j(k'')$, which is negative when $k'' < k''(min_j)$ and positive otherwise. The entire ordering process, which is characterized by the evolving set of k indices, has strong similarities with a machine learning algorithm approach [Yuhao Li 2019]

We are now able to write $g_j(k'')$ and to optimize $R_{min,j}$ by forcing g_{j1}/g_{j2} to be a constant, as we did before.

Reference S2

[Yuhao Li 2019] Yuhao Li, Yangyang Kong, Jinlin Peng, Chuanbin Yu, Zhi Li, Penghui Li, Yunya Liu, Cun-Fa Gao, Rong Wu, Rapid identification of two-dimensional materials via machine learning assisted optic microscopy, *Journal of Materiomics* 2019, **5**, 413e421

Supplementary S3

Figures S3a and S3b show two images of the same multilevel hBN stack with respectively direct and inverted contrast for better visibility of the 30 different zones. Figure 3c-e shows the $f(m)$ results independently obtained with each channel after applying the procedure explained in the main text. The $m_{min,j}$ values found for the red, green and blue channels are respectively 29, 20 and 10.5, to compare with the [24, 14, 7.5] previous ones. This difference reveals a change in instrumental parameters, including the exact composition of the ARA substrate. It shows that from one experiment

to another with different settings, the colors in the images or the measured single channel intensities cannot be directly compared. From this simple remark we can suspect huge difficulties when fitting reflected intensities with an absolute model.

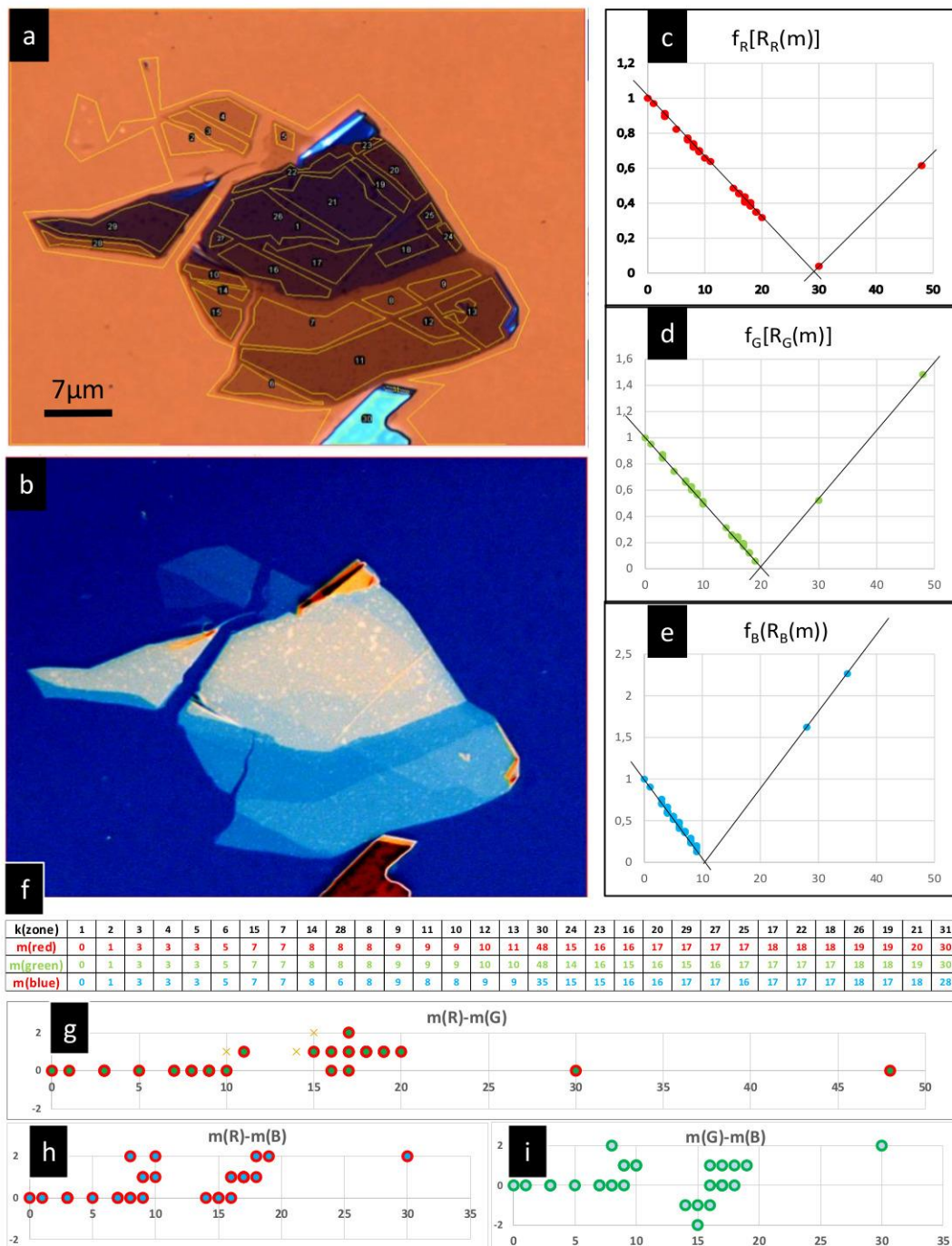


Figure S3 a: a complex hBN stack with many internal steps defining 30 measurement zones at the micron scale. The full height of the image corresponds to 45 μm ; b: same with inverted contrast for complementary zone recognition; c: linearized reflectivity as a function of m on the red channel; d-e : same for the green and the blue channels; f: number of layers as independently found from each color channel; g: difference in the m evaluation from the red and the green channels for all numbers from 0 to 50; h: difference in the m evaluation from the red and the blue channels, limited to the first 30 layers; i: difference in the m evaluation obtained from the green and the blue channels, limited to the first 30 layers.

The number of layers that was independently determined on each channel for each zone using the χ^2 minimization is reported in Figure S3f. Thanks to thickness quantization, the agreement between the red and the green channels is perfect below 11 layers and within a one layer uncertainty up to 48 monolayers. Several two-layer misfits are observed between the blue and the two other channels above 8 monolayers. The highest thickness is also strongly underestimated on the blue. This is consistent with respectively a noisier signal and a weakened linearity of $f_B(R_B)$ with $e(k)$ far from $e_{min,B}$. A high precision in the estimation of m is especially important for small m because the specific properties of 2D materials is manifested in low stacks, and critically depend on m . Our method proves to be very effective in the low m range.

Applying afterwards the χ^2 minimization to the data presented in Figure S1, we found the same $m(k)$ attribution as the one previously obtained with the folded sheet anchor in the discussion of Figure 2. All the data are therefore consistent.

Supplement S4

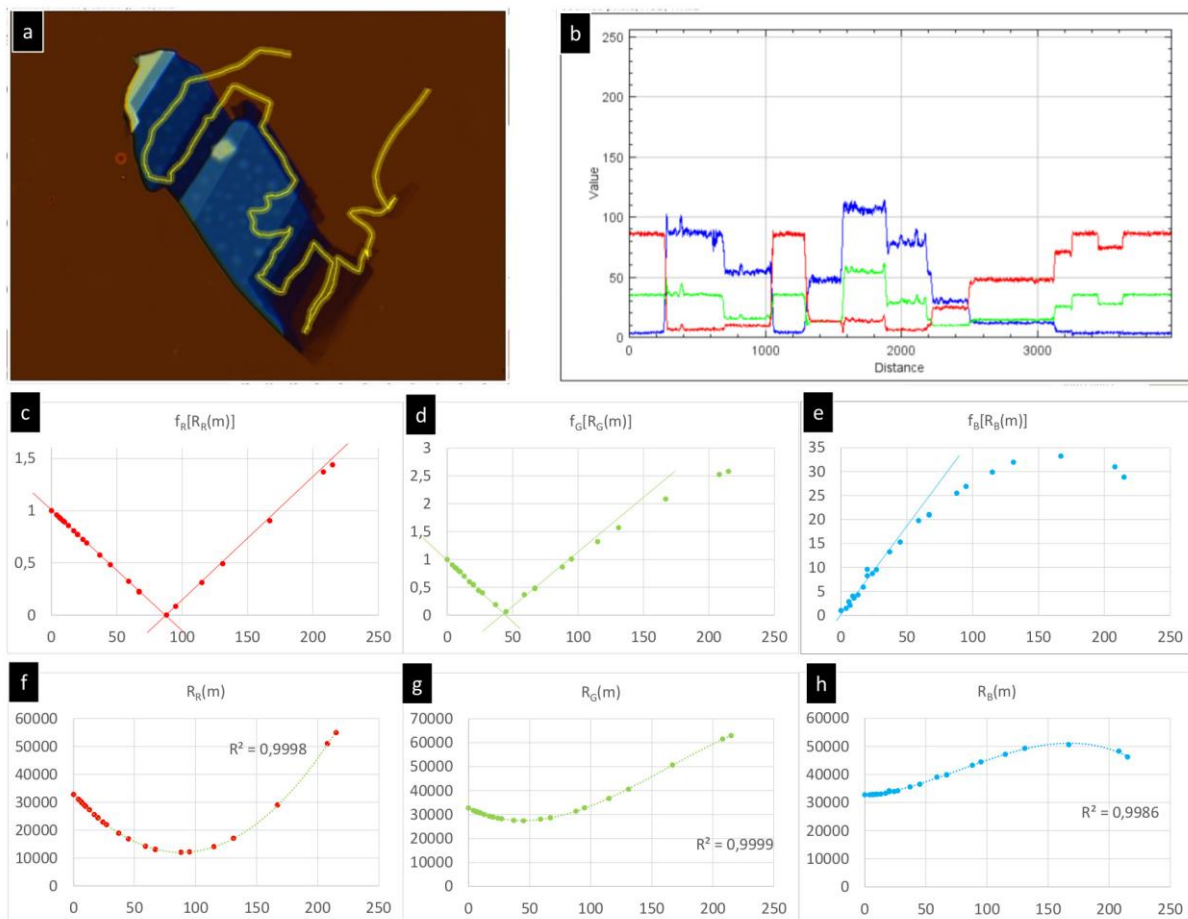


Figure S4. a: part of the image used in the measurement, 32 μm high, with a ten pixels wide yellow path covering some of the domains; b: RGB profiles along the yellow path; c-e: $f_j(m)$ for the red, green and blue channel. Non linearities appear as a deviation from the symmetric straight lines with respect to the minimum; f-h: $R_j(m)$ for the red, green and blue channel. The dotted lines are the best

polynomial fits obtained using either a second order (Red) or a third order polynomial (Green and Blue).

The hBN sample and the ARA surface used in Figure 3 and Figure S4 are the same. Only the size of the aperture hole is different, leading to significant variations in $R_{min,j}$ on the green and the red channels. This illustrates once more the difficulty that we would expect in fitting the experimental data with a multiparameter numerical model. For the sake of clarity, only a part of the used image is shown in Fig.S4a, with a yellow path drawn in it also covering only a part of the measured domains. The intensity profiles along this path are shown in Fig.S4b. Their diversity illustrates the richness of the colorimetric information. The measurements cover a much larger thickness range than in all other examples in this work. The $f_j(m)$ results are displayed for the three channels in Figures S4c-e. They extend far beyond the linear regime on the blue, with a maximum around 167 layers, while they stay quite linear on the red. The same results are shown as $R_j(m)$ in Figures S4f-h, with a fitted polynomial through the data. $R_R(m)$ is still well described by the basic parabola, as demonstrated by the R^2 quality factor, while it is no more effective with the green and the blue data. Interestingly, they may still be described by a third order polynomial (with the corresponding R^2 in the Figure), which opens possibilities to extend our analysis to thicker samples. Due to the properties of the f_j transform, the maxima of $R_B(m)$ and $f_B(m)$ are in correspondence (obtained for the same m). The distance between the blue minimum, close to zero, and the blue maximum corresponds to the optical thickness $\lambda/4$, with λ the wavelength of light. The blue sensor in our camera is peaked at 470 nm, which gives $\lambda/4 = 117,5$ nm. Dividing this quantity by the hBN refractive index at this wavelength, namely 2.17, gives a physical thickness 54 nm at the maximum. With 0.333 nm the thickness of one monolayer, it corresponds to 162 monolayers. Subtracting the $m_{min} = 3$ monolayers found in the analysis for the position of the blue minimum, we finally expect 159 monolayers from interference theory where we counted 167 from our experiment. The difference is within 5%. Therefore, there is absolutely no doubt that the monolayer unit was correctly identified. Alternatively, comparing the extracted optical thickness $\lambda/4$ (more accurately using spectral filtering) and the corresponding physical thickness (from m counting and knowledge of monolayer thickness), we find that our self-calibrating procedure can be utilized to evaluate the hBN (or any other 2D material) refractive index at the given wavelengths employed in the imaging.

Supplement S5

In Figure S5, we present the same folded sheet as in main text but here focus on the contaminant spots which clearly appear in the optical microscopy. Interestingly, their contrast is very different depending on the channel considered. They appear as bumps in the blue channel and as holes in the red and green channels, with an amplitude up to 4 equivalent monolayers. This originates from their different nature (attributed to polymer residues or atmospheric hydrocarbons) and hence different refractive index compared to hBN. Their absolute height cannot be directly scaled to the m counting calibration and thus cannot be quantitatively evaluated. However, their impact on the measured average value is given by their apparent height, i-e their intensity amplitude, and becomes important for small flake areas. For accurate m counting, contaminated regions can be removed from the selected areas used for optical signal averaging, as done in Figure 3 analysis in main text. We finally emphasize on the strong optical contrast shown by these contaminants in our imaging compared to usual optical microscopy.

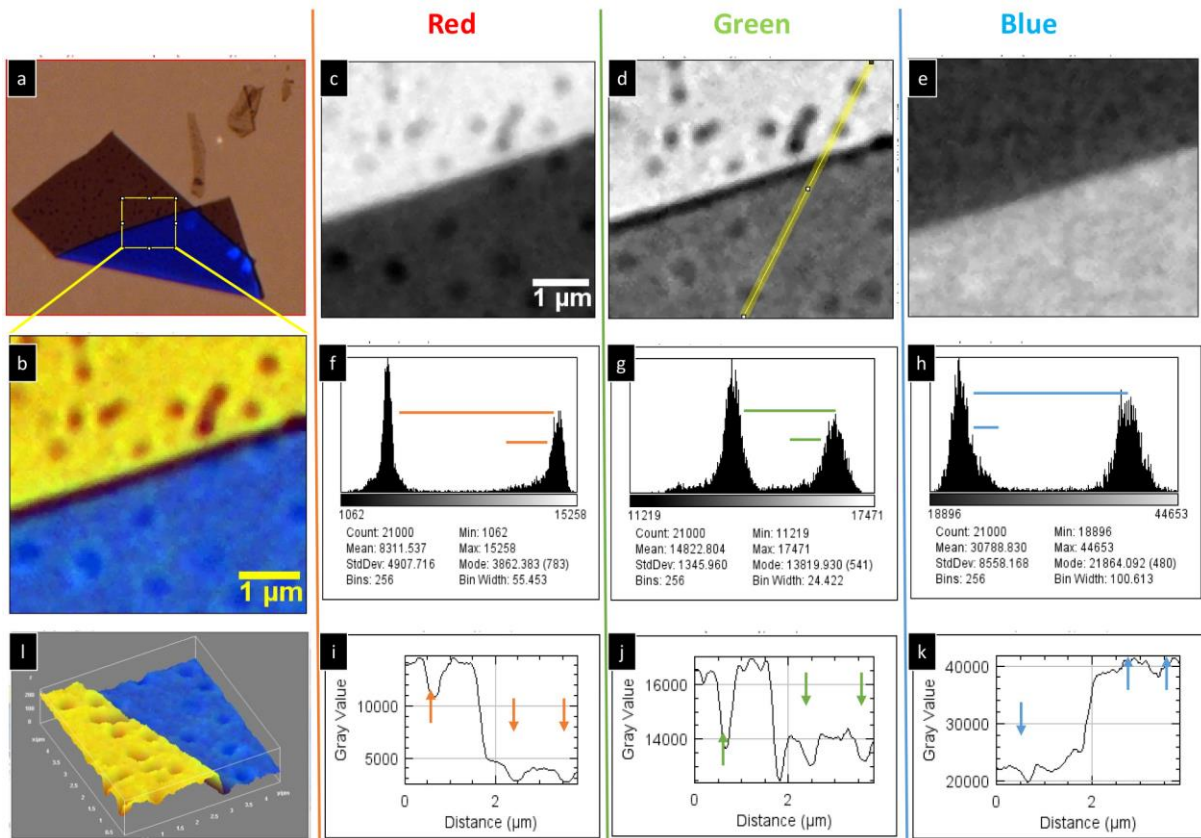


Figure S5 From a to b: Enlargement of the one sheet four layers step, followed by contrast optimization; c-e: the three channels of Figure 5b, displayed using a linear grey scale – with the definition in d of an ten pixel wide yellow line crossing three defects; f-h: respective histograms of the images d-e, with colored horizontal lines to help comparing the amplitude of the defects and that of the 4 layers step; i-k: Intensity profiles along the yellow line defined in d, with arrows pointing the marks of the defects; l: 3D representation of b, with the green channel intensity converted in height.